

Nonlinear parametrically excited surface waves in surfactant-covered thin liquid films

By O. K. MATAR¹, S. KUMAR² AND R. V. CRASTER³

¹Department of Chemical Engineering and Chemical Technology,
Imperial College London, SW7 2AZ, UK

²Department of Chemical Engineering and Materials Science, University of Minnesota, 151 Amundson Hall, 421 Washington Ave. SE, Minneapolis, MN 55455, USA

³Department of Mathematics, Imperial College London, SW7 2AZ, UK

(Received 5 October 2003 and in revised form 9 August 2004)

The effect of gravity modulation on the nonlinear evolution of long-wavelength disturbances at the free surface of a surfactant-covered thin liquid layer is studied. The surfactants, which are assumed to be insoluble, give rise to interfacial concentration gradients and associated Marangoni flow in the underlying liquid film. A coupled system of lubrication-theory-based evolution equations for the film height and surfactant concentration is solved numerically using spectral methods. Previous work using Floquet theory had determined that small-amplitude long-wavelength disturbances are destabilized by gravity modulation in the presence of surfactant; uncontaminated films were found to be linearly stable. Our numerical results indicate that uncontaminated free surfaces are destabilized by nonlinearities and exhibit a harmonic response. The interface exhibits complex dynamics during a forcing cycle, characterized by numerous coalescence events between thickened fluid ridges leading to coarsening. The presence of surfactant-induced Marangoni flow gives rise to a harmonic response, larger scale fluid structures of reduced amplitude, less frequent coalescence events, and less complicated film dynamics.

1. Introduction

The adsorption of surface-active agents, or surfactants, at the free surface of a liquid leads to a reduction in surface tension (Edwards, Brenner & Wasan 1991). Surfactant concentration variations, however, lead to surface tension gradients that drive a so-called Marangoni flow in the underlying liquid from regions of low to high surface tension, which may be undesirable for certain applications such as coating (Scriven & Sternling 1964) and crystal growth (Carpenter & Homsy 1985). Free surfaces in fluid systems are also subject to time-dependent gravitational forces in microgravity environments. The forces, which may assume the form of vertical vibration, are capable of exciting standing free-surface waves; these waves have received considerable attention in the literature since the early work of Faraday (1831).

Wave formation on vertically vibrated liquid layers has been investigated for inviscid (Benjamin & Ursell 1954; Miles & Henderson 1990), Newtonian (Kumar 1996; Perlín & Schultz 2000), and non-Newtonian fluids (Kumar 1999) in the presence of sinusoidal modulation of a mean gravity, with Floquet theory applied to obtain time-periodic solutions of the linearized governing equations. These solutions correspond to standing waves, obtained above a finite frequency-dependent critical vibration

amplitude for viscous liquids beyond which viscous dissipation is overcome. Since no such amplitude exists in the case of inviscid fluids, due to the absence of viscous dissipation, a unique critical disturbance wavenumber cannot be predicted in this case. Comparisons carried out between theory and experiment for the viscous case in terms of the critical amplitude and wavenumber for both Newtonian (Bechhoefer *et al.* 1995) and non-Newtonian liquids (Raynal, Kumar & Fauve 1999; Wagner, Muller & Knorr 1999) yielded excellent agreement.

Recent investigations of nonlinear Faraday waves have involved direct numerical simulations of the two-dimensional Navier–Stokes equations. Two-dimensional standing waves between semi-infinite inviscid fluids were studied as a function of the Atwood number by Wright, Yon & Pozrikidis (2000) using the boundary integral method and a vortex-sheet-based method; viscous dissipation was taken into consideration using a linear damping coefficient in the momentum conservation equations. This study shows the emergence of travelling waves in the presence of strong forcing, which then collide and result in the formation of large ridges. The results of Wright *et al.* (2000) also illustrated a transition in the observed response from linear stability to plume formation and droplet ejection with increasing Atwood number. In the case of viscous fluids, two-dimensional Navier–Stokes simulations have provided a detailed picture of the nature of the bifurcation to standing waves and of the velocity field beneath them (Murakami & Chikano 2001), an elucidation of the waves resulting from the interactions between different modes (Chen 2002) (although only strictly valid in the weakly nonlinear regime), and stability maps as a function of the forcing amplitude, the Froude number, and the initial film thickness (Ubal, Giavedoni & Saita 2003). In the latter study, it was shown that for sufficiently thin films (equal to 10^{-5} m), viscous dissipation at the solid boundary strongly influences the flow. Although most experimental studies show that the standing waves respond subharmonically to the driving, for highly viscous fluids and low-frequency forcing (Muller *et al.* 1997) harmonic responses are observed.

The theoretical studies mentioned above involve uncontaminated interfaces having a uniform surface tension. What effect does gravity modulation, then, have on disturbances at a contaminated free surface? Recently, this question was considered by Kumar & Matar (2004), who performed a linear stability analysis to account for surface tension variations due to the presence of an insoluble surfactant adsorbed at the air–liquid interface. This analysis, which is valid for fluids of arbitrary depth and viscosity, neglected the effects of lateral boundaries. It was found that surfactants have a damping effect, raising the critical vibration amplitude needed to excite surface waves relative to its value for an uncontaminated surface. For sufficiently large Marangoni numbers, surfactants also increase the critical wavenumber, suggesting that surfactants could reduce the size of droplets ejected from the standing waves.

Kumar & Matar (2002) examined the response of a vertically vibrated surfactant-covered thin liquid film to small-amplitude long-wavelength disturbances using lubrication theory. They considered the case in which the thickness of the liquid layer is much smaller than the wavelength of the interfacial disturbance, thereby allowing a separation of length scales that was not possible in Kumar & Matar (2004). They derived a coupled system of nonlinear partial differential equations describing the free-surface height and the surfactant concentration as a function of time and the horizontal spatial coordinate. Using Floquet theory, they found that the presence of surfactant is destabilizing; these disturbances, however, are stable in the case of uncontaminated films. Additionally, they found that increasing the relative significance of the Marangoni stresses, capillarity, body forces, and surfactant diffusivity is stabilizing.

It is worthy of note that the asymptotic analysis of Kumar & Matar (2002) is fundamentally different from one recently reported in the literature (Cerde & Tirapegui 1999; Cerde, Rojas & Tirapegui 2001) in which the linearized Navier–Stokes equations and boundary conditions are used to develop an evolution equation for interfacial disturbances. Solutions are obtained that are non-local in time, and which are expanded in terms of an infinite series of time derivatives. Truncation of this series leads to a Mathieu equation which does predict that vibration will destabilize surface disturbances. This analysis does not appear to be a traditional lubrication analysis like the one adopted here and by Kumar & Matar (2002).

The work of Kumar & Matar (2002) allows the determination of the conditions for instability and is, therefore, capable of describing the flow near the onset of instability only, before nonlinearities become significant. In order to elucidate the system dynamics beyond the onset of unstable flow, however, solutions of the fully nonlinear governing equations must be determined. The goal of the present work is therefore to examine the evolution of clean and surfactant-covered films in the nonlinear regime using transient numerical simulations of the equations derived by Kumar & Matar (2002). Note that it is far easier to obtain numerical solutions of the evolution equations in the present work than it is to solve the two-dimensional Navier–Stokes equations (Wright *et al.* 2000; Murakami & Chikano 2001; Ubal *et al.* 2003). Thus this lubrication-theory-based formulation can serve as a simpler model, which may be useful for understanding the behaviour observed in thin films of viscous liquids.

The rest of this paper is organized as follows. A brief review of the problem formulation is provided in §2; details can be found in Kumar & Matar (2002). In §3, we validate the numerical procedure used to carry out the computations against the predictions of linear theory, and devote the remainder of this section to a discussion of the numerical results in the nonlinear regime of the instability. Finally, concluding remarks are provided in §4.

2. Problem formulation

We consider a thin layer of an incompressible Newtonian liquid of density ρ and viscosity μ , initially covered by a monolayer of insoluble surfactant having a uniform concentration. This layer rests on an impermeable horizontal support which undergoes vertical sinusoidal oscillations of amplitude a and frequency ω . We use the coordinate system (x, z) and the velocity field $\mathbf{u} = (u, 0, w)$ to describe the two-dimensional dynamics, where x and z denote the horizontal and vertical coordinates and u and w the associated velocity components, respectively. The liquid–solid interface and undisturbed air–liquid interface are located at $z=0$ and $z=\mathcal{H}$, respectively. The effects of lateral boundaries are neglected as are the dynamics of the essentially inviscid air, which overlies the liquid layer.

The equations of momentum and mass conservation are respectively given by

$$\rho(\mathbf{u}_t + \mathbf{u} \cdot \nabla \mathbf{u}) = -\nabla p + \mu \nabla^2 \mathbf{u} - \rho B(t) \mathbf{e}_z, \quad \nabla \cdot \mathbf{u} = 0, \quad (2.1)$$

in which t denotes time, p is the pressure, the function $B(t) = g - a \cos(\omega t)$ is the modulated gravity wherein g is the mean gravitational acceleration, and \mathbf{e}_z is the unit vector in the z -direction.

Solutions of these governing equations are obtained subject to appropriate boundary conditions. The shear stress balance at the air–liquid interface (Deen 1998), located

at $z = h(x, t)$, is expressed by

$$\mathbf{t} \cdot \boldsymbol{\pi} \cdot \mathbf{n} = \mathbf{t} \cdot \nabla_s \sigma, \quad (2.2)$$

while the normal stress balance is given by

$$\mathbf{n} \cdot \boldsymbol{\pi} \cdot \mathbf{n} = -\sigma \kappa. \quad (2.3)$$

Here, σ is the surface tension, κ is the curvature, \mathbf{t} and \mathbf{n} are the tangent and normal unit vectors to the interface, respectively, and $\nabla_s = (\boldsymbol{\delta} - \mathbf{n}\mathbf{n}) \cdot \nabla$ is the surface gradient operator in which $\boldsymbol{\delta}$ is the identity tensor. The tensor $\boldsymbol{\pi}$ is expressed by

$$\boldsymbol{\pi} = -[p - \rho B(t)h]\boldsymbol{\delta} + \mu(\nabla \mathbf{u} + (\nabla \mathbf{u})^T). \quad (2.4)$$

The kinematic boundary condition at $z = h(x, t)$ is given by

$$(\partial_t + u_s \partial_x)h = w_s, \quad (2.5)$$

where u_s and w_s denote the horizontal and vertical components of the velocity evaluated at $z = h$. The equation of mass conservation of insoluble surfactant is given by

$$\Gamma_t + \nabla_s \cdot (\mathbf{u}_s \Gamma) + (\mathbf{u} \cdot \mathbf{n})(\nabla_s \cdot \mathbf{n})\Gamma = \mathcal{D} \nabla_s^2 \Gamma, \quad (2.6)$$

where Γ is the surfactant surface concentration, $\mathbf{u}_s = (\boldsymbol{\delta} - \mathbf{n}\mathbf{n}) \cdot \mathbf{u}$ and \mathcal{D} is the surfactant surface diffusion coefficient (Stone 1990). Finally, no-slip and no-penetration conditions are applied at the support, located at $z = 0$:

$$u = w = 0. \quad (2.7)$$

In order to render the above equations dimensionless, the following scaling is chosen:

$$u = (\omega \mathcal{H}) \tilde{u}, \quad w = (\epsilon \omega \mathcal{H}) \tilde{w}, \quad x = L \tilde{x}, \quad (z, h) = \mathcal{H}(\tilde{z}, \tilde{h}), \quad (2.8)$$

$$t = (1/\omega) \tilde{t}, \quad p = (\mu \omega L / \mathcal{H}) \tilde{p}, \quad (2.9)$$

where the tilde denotes dimensionless quantities. Here, we shall assume that the ratio of the film depth, \mathcal{H} , to the wavelength of the interfacial disturbance, L , is $\epsilon = \mathcal{H}/L \ll 1$. For the surfactant concentration, Γ , and surface tension, σ , we choose the following scaling:

$$\Gamma = \Gamma_m \tilde{\Gamma}, \quad \sigma = \sigma_m + \tilde{\sigma} \mathcal{S}, \quad (2.10)$$

where Γ_m denotes the mean surfactant concentration and σ_m is the surface tension corresponding to Γ_m . The spreading pressure is given by $\mathcal{S} = \sigma_0 - \sigma_m$, where σ_0 denotes the value of the surface tension for an uncontaminated liquid surface. We assume that the surfactant concentration is sufficiently dilute to permit use of a linear equation of state:

$$\sigma = \sigma_0 + \left(\frac{\partial \sigma}{\partial \Gamma} \right)_{\Gamma=0} \Gamma. \quad (2.11)$$

Substitution of these scalings into the equations of mass and momentum conservation, the boundary conditions at $z = 0$ and $z = h$, and the surfactant equation of state, yields a set of dimensionless equations to leading order in ϵ . (The tilde is henceforth dropped.) We now demote the inertial terms in the equations of momentum

conservation by setting $t \rightarrow \epsilon t$. All variables are then expanded in powers of ϵ and the leading-order equations are manipulated to yield a set of evolution equations for h_0 and Γ_0 , where the subscript '0' denotes the leading-order contribution. As the details are given in Kumar & Matar (2002), we simply quote the final results below.

The evolution equations are

$$h_{0t} = \left(\frac{1}{2} \mathcal{M} h_0^2 \Gamma_{0x} + \frac{1}{3} h_0^3 [B(t) h_{0x} - \mathcal{C} \mathcal{M} h_{0xxx}] \right)_x, \quad (2.12)$$

$$\Gamma_{0t} = \left(\mathcal{M} h_0 \Gamma_0 \Gamma_{0x} + \frac{1}{Pe} \Gamma_{0x} + \frac{1}{2} \Gamma_0 h_0^2 [B(t) h_{0x} - \mathcal{C} \mathcal{M} h_{0xxx}] \right)_x, \quad (2.13)$$

where we have used $\sigma_0 = 1 - \Gamma_0$. Here, \mathcal{M} is a Marangoni parameter given by

$$\mathcal{M} \equiv \frac{\epsilon \mathcal{S}}{\mu \omega \mathcal{H}}, \quad (2.14)$$

and $B(t) = \mathcal{B} - \mathcal{A} \cos(t)$ represents a modulated gravitational acceleration where

$$\mathcal{A} \equiv \frac{\epsilon \rho a \mathcal{H}}{\mu \omega} \quad (2.15)$$

is the dimensionless amplitude of sinusoidal acceleration and

$$\mathcal{B} \equiv \frac{\epsilon \rho g \mathcal{H}}{\mu \omega} \quad (2.16)$$

provides a measure of the significance of mean gravitational forces. The parameter \mathcal{C} , given by

$$\mathcal{C} \equiv \frac{\epsilon^2 \sigma_m}{\mathcal{S}}, \quad (2.17)$$

is an inverse capillary number reflecting the importance of capillarity. In (2.13), Pe , which represents the ratio of surfactant transport by convection to that by surface diffusion, is expressed by

$$Pe \equiv \frac{\omega \mathcal{H} L}{\mathcal{D}}, \quad (2.18)$$

in which \mathcal{D} is a constant surfactant surface diffusion coefficient.

For the case where surfactants are absent, we set $\Gamma_0 = 0$ in (2.12) and (2.13), which yields a single evolution equation for the uncontaminated film thickness, $h_0^{(o)}$:

$$h_{0t}^{(o)} = \left(\frac{1}{3} h_0^{(o)3} [B^{(o)}(t) h_{0x}^{(o)} - \tilde{\mathcal{C}}^{(o)} h_{0xxx}^{(o)}] \right)_x, \quad (2.19)$$

where the superscript '(o)' denotes the surfactant-free case; here $B^{(o)}(t) = \mathcal{B}^{(o)} - \mathcal{A}^{(o)} \cos(t)$. The scalings have also been changed: $\mathcal{S} \rightarrow \sigma_0$, and $\sigma_m \rightarrow \sigma_0$. Hence, the dimensional surface tension has been scaled on the value of the surface tension associated with the clean interface, σ_0 . As a result, \mathcal{M} and \mathcal{C} now become $\mathcal{M} \rightarrow \mathcal{M}^{(o)} = \epsilon \sigma_0 / \mu \omega \mathcal{H}$ and $\mathcal{C} \rightarrow \mathcal{C}^{(o)} = \epsilon^2$. The new dimensionless group appearing in (2.19), $\tilde{\mathcal{C}}^{(o)}$, is now expressed by $\tilde{\mathcal{C}}^{(o)} = \mathcal{C}^{(o)} \mathcal{M}^{(o)} = \epsilon^3 \sigma_0 / \mu \omega h = \epsilon^3 / Ca$, where Ca is a capillary number; thus $\tilde{\mathcal{C}}^{(o)}$ is an inverse capillary number. The remaining dimensionless groups $\mathcal{A}^{(o)}$ and $\mathcal{B}^{(o)}$ are unchanged from (2.15) and (2.16), respectively. Note that the subscript zero notation is henceforth suppressed.

In the present work, we focus on the nonlinear evolution of the leading-order equations, which is discussed next, following a brief examination of the linear stability characteristics of the system.

3. Discussion of results

In this section, we present some further results of a linear stability analysis of the evolution equations governing the dynamics of the film thickness and surfactant concentration. We then present a discussion of the results obtained via numerical integration of (2.12) and (2.13). The uncontaminated free surface case is considered first followed by that of a surfactant-covered interface; this is preceded by a brief description of the numerical method employed.

3.1. Linear stability analysis

In order to validate the predictions of the numerical procedure and to gain insight into the problem, we linearize the lubrication equations developed above, (2.12), (2.13) and (2.19), and examine their stability to small perturbations. In the presence of surfactant, we linearize (2.12) and (2.13) about $h = 1$ and $\Gamma = 1$ by introducing the expansion

$$(h, \Gamma)(x, t) = 1 + (H, G)(t) e^{ikx}, \quad (3.1)$$

where k is a dimensionless wavenumber. In the absence of surfactant, the surface deformation, $h^{(o)}$, is expanded similarly with H being replaced by $H^{(o)}$.

The linearized version of (2.19) is

$$H_t^{(o)} = \frac{1}{3}k^2 \mathcal{A}^{(o)} \cos(t) H^{(o)} - \frac{1}{3}k^2 (\mathcal{B}^{(o)} + \tilde{\mathcal{C}}^{(o)} k^2) H^{(o)}. \quad (3.2)$$

This equation can be integrated from 0 to t to yield

$$H^{(o)} = H^{(o)}(t = 0) \exp \left[\frac{1}{3}k^2 \mathcal{A}^{(o)} \sin(t) - \frac{1}{3}k^2 (\mathcal{B}^{(o)} + \tilde{\mathcal{C}}^{(o)} k^2) t \right]. \quad (3.3)$$

Inspection of (3.3) reveals that disturbances to the free surface in the uncontaminated case considered in the asymptotic limit $\epsilon \ll 1$ decay to zero as $t \rightarrow \infty$ (Kumar & Matar 2002), indicating that instability and standing wave generation will not occur. Note that Kumar & Matar (2002) had obtained instability in the long-wavelength limit in the presence of van der Waals forces only. The lack of instability in the absence of these forces may be a consequence of the fact that inertial effects are not included in the evolution equation. Linear stability analyses of the full Navier–Stokes equations indicate that vertical vibration will always produce instability. However, these analyses include inertial effects and are not restricted to long-wavelength disturbances. Nevertheless, exploring the nonlinear behaviour of the evolution equation is still of interest because of the possibility that inherently nonlinear instabilities exist.

The linearized version of (2.12) and (2.13) is

$$H_t = \frac{1}{3}k^2 \mathcal{A} \cos(t) H - \frac{1}{3}k^2 (\mathcal{B} + \mathcal{C} \mathcal{M} k^2) H - \frac{1}{2}k^2 \mathcal{M} G, \quad (3.4)$$

$$G_t = \frac{1}{2}k^2 \mathcal{A} \cos(t) H - \frac{1}{2}k^2 (\mathcal{B} + \mathcal{C} \mathcal{M} k^2) H - k^2 \left(\mathcal{M} + \frac{1}{Pe} \right) G, \quad (3.5)$$

which is a pair of coupled first-order ordinary differential equations with time-dependent coefficients. In the absence of vibration, the coefficients are no longer time

dependent and disturbances of all wavenumbers decay for all values of \mathcal{B} , \mathcal{C} , and Pe (Kumar & Matar 2002). In the presence of vibration, however, time-periodic solutions corresponding to standing waves are expected. In order to study such solutions, we apply Floquet theory as detailed by Kumar & Matar (2002). We provide below only a brief description of the procedure and quote the relevant results.

The functions $H(t)$ and $G(t)$ are replaced by

$$H(t) = e^{(s+i\alpha)t} \sum_{n=-\infty}^{\infty} H_n e^{int}, \quad G(t) = e^{(s+i\alpha)t} \sum_{n=-\infty}^{\infty} G_n e^{int}, \quad (3.6)$$

where s is the real-valued growth rate and the value of α indicates whether the response of the standing waves to the modulation is subharmonic ($\alpha = 1/2$) or harmonic ($\alpha = 0$). Substitution of (3.6) into (3.4) and (3.5) and subsequent elimination of G_n then yields the following recursion relation:

$$A_n H_n = \mathcal{A}(H_{n+1} + H_{n-1}), \quad (3.7)$$

wherein

$$A_n = \frac{2(s + i(\alpha + n) + \frac{1}{3}k^2 D_n - \frac{1}{4}k^4 \mathcal{M} D_n / C_n)}{\frac{1}{3}k^2 - \frac{1}{4}k^4 \mathcal{M} / C_n}, \quad (3.8)$$

in which

$$C_n = s + i(\alpha + n) + \left(\mathcal{M} + \frac{1}{Pe} \right) k^2, \\ D_n = \mathcal{B} + \mathcal{C} \mathcal{M} k^2,$$

which can be truncated at a finite value of n , \mathcal{N} , and converted into a matrix eigenvalue problem (Kumar & Tuckerman 1994). Solution of this eigenvalue problem for $s = 0$ gives rise to a set of ‘tongue-like’ neutral stability curves in the (k, \mathcal{A}) -plane. The critical vibration amplitude required to excite standing waves can be determined from the tongue tip which is closest to the k -axis; this will also yield the critical wavenumber.

Figure 1 shows neutral stability curves generated with $\mathcal{N} = 20$ for $\mathcal{M} = 0.1$ –100 with the rest of the parameter values held fixed at $\mathcal{B} = 0.16$, $\mathcal{C} = 0.0075$, and $Pe = 6.3 \times 10^5$; harmonic and subharmonic responses can be clearly seen in figure 1. The curve for each type of response has a tongue-like shape that, in fact, comprises a series of finer tongue-like curves. Inspection of figure 1 reveals that for all values of \mathcal{M} , the tongue having the lowest amplitude corresponds to a harmonic response, while the critical amplitude (wavenumber) increases (decreases) with increasing \mathcal{M} ; the increase in k_c with decreasing \mathcal{M} is consistent with the fact that a thin surfactant-free film is linearly stable. Thus the results shown in figure 1 indicate that although the presence of surfactant is destabilizing, increasing the relative significance of Marangoni stresses exerts a stabilizing effect. Note further that there probably exists a limit of small \mathcal{M} for a given set of parameter values beyond which the value of k_c becomes sufficiently large to render lubrication theory invalid.

As discussed by Kumar & Matar (2002), the critical vibration amplitude decreases with decreasing \mathcal{B} and \mathcal{C} , as expected, since both gravity and surface tension act as restoring forces. The critical amplitude increases, however, with decreasing Pe , since more rapid diffusion restores the surfactant concentration to its initially uniform state. This reduces the problem to that of an uncontaminated interface with modified

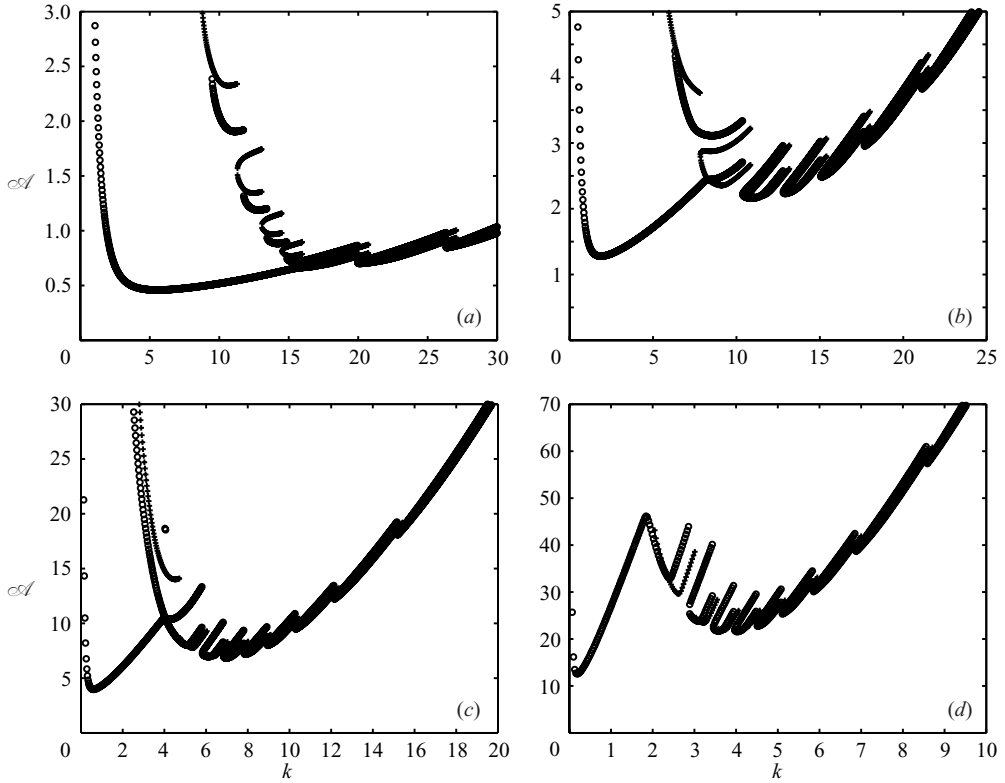


FIGURE 1. Neutral stability curves, \mathcal{A} vs. k , for (a) $\mathcal{M} = 0.1$; (b) $\mathcal{M} = 1$; (c) $\mathcal{M} = 10$; (d) $\mathcal{M} = 100$. The values of the other parameters are $\mathcal{B} = 0.16$, $\mathcal{C} = 0.0075$, and $Pe = 6.3 \times 10^5$. Subharmonic and harmonic responses are represented by pluses and circles, respectively.

mean surface tension, which is stable. In all cases considered, the critical wavenumber decreases whenever the critical amplitude increases.

The response of the air–liquid interface and surfactant concentration to variations in the amplitude of gravity modulation is shown in figure 2 for the same parameters as those used to generate figure 1(c) and $k = 1$. Clearly, $H(t)$ and $G(t)$ exhibit harmonic oscillations, which grow (decay) above (below) a critical value of $A \approx 4.37$ for this set of parameters. Insight into the destabilizing mechanism may be gained via inspection of figure 3(a), which depicts an enlarged view of figure 2. The amplitude of the perturbation in the surfactant concentration, $G(t)$, is negative over a range of the forcing period, during which $H(t)$ is positive. This implies that the perturbations in the film thickness and surfactant concentration are out of phase over this duration, i.e. film thickness minima coincide with surfactant concentration maxima. Marangoni stresses then act to spread the surfactant from regions of high concentration to low concentration, which leads to instability. This mechanism is, of course, absent in the uncontaminated case, as shown in figure 3(b), which illustrates the harmonic response of a surfactant-free case to gravity modulation. Over the remaining duration of a forcing cycle, however, $H(t)$ and $G(t)$ have the same sign, implying that Marangoni stresses can also be stabilizing. This can be related to the establishment of regions of relatively high concentration at the peaks of the perturbed free surface, leading to

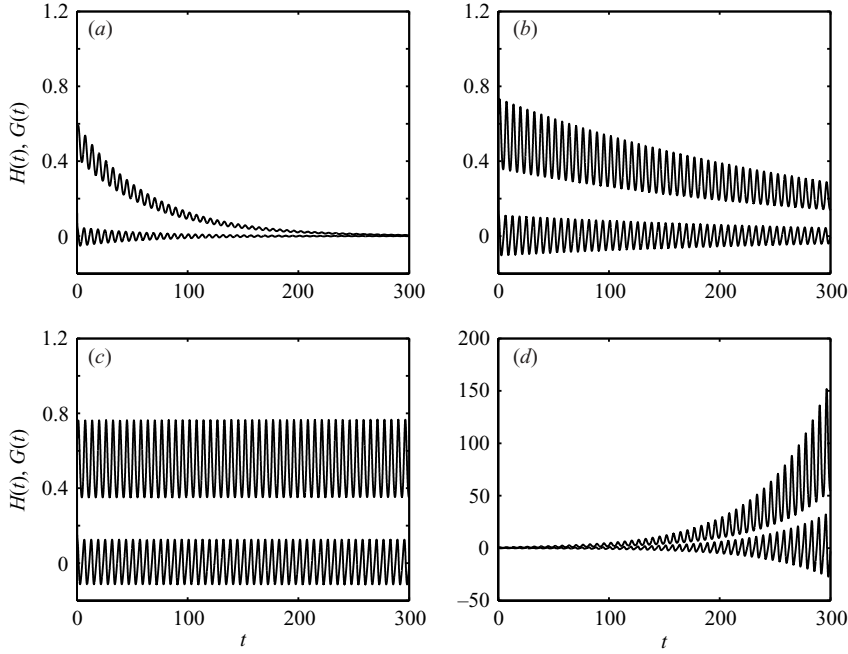


FIGURE 2. The effect of increasing the forcing amplitude, \mathcal{A} , on $H(t)$ (upper curves) and $G(t)$ for the same parameter values as in figure 1(c) and $k=1$. (a) $A=2$, (b) $A=4$, (c) $A=4.37$, (d) $A=6$.

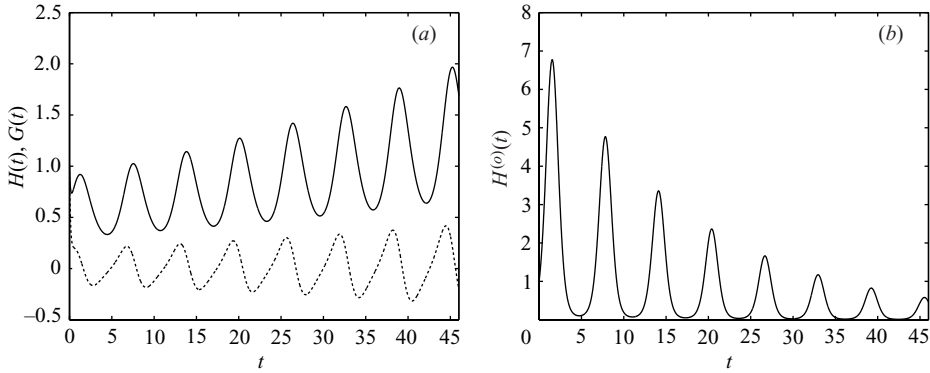


FIGURE 3. Temporal variation of (a) $H(t)$ (solid line) and $G(t)$ (dashed line), and (b) $H^{(0)}(t)$, for the same parameter values as in figure 2.

Marangoni flow from high to low concentration regions, i.e. from the crests to the troughs.

In order to gain further insight into the nature of the flow, we re-express (3.4) and (3.5) as

$$\frac{1}{2} \frac{H_t^2}{H^2} = \frac{1}{3} k^2 \mathcal{A} \cos(t) - \frac{1}{3} k^2 (\mathcal{B} + \mathcal{C} \mathcal{M} k^2) - \frac{1}{2} k^2 \mathcal{M} G/H, \quad (3.9)$$

$$\frac{1}{2} \frac{G_t^2}{G^2} = \frac{1}{2} k^2 \mathcal{A} \cos(t) H/G - \frac{1}{2} k^2 (\mathcal{B} + \mathcal{C} \mathcal{M} k^2) H/G - k^2 \left(\mathcal{M} + \frac{1}{Pe} \right). \quad (3.10)$$

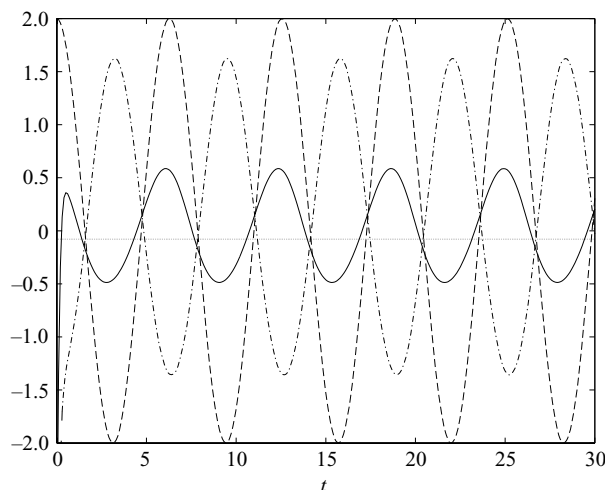


FIGURE 4. Temporal variation of the terms contributing to the growth or decay of perturbations in the film thickness, I_1 (dashed line), I_2 (grey line), and I_3 (dot-dashed line), as well as the instantaneous linear growth rate, $H_t^2/2H^2$ (solid line); I_1 , I_2 , and I_3 correspond to the three terms on the right-hand side of in (3.9). The parameter values remain unchanged from figure 3(a).

The left-hand sides of these equations may be identified as the instantaneous growth rates of disturbances in the film thickness and surfactant concentration. The first, second, and third terms on the right-hand side of (3.9), henceforth referred to as I_1 , I_2 , and I_3 , respectively, correspond to gravity modulation, mean gravity and capillarity, and Marangoni stresses. The first and second terms on the right-hand side of (3.10) correspond to gravity modulation and mean gravity and capillarity, while the third term is related to Marangoni stresses and surface diffusion. We shall concentrate, however, on the predictions of (3.9).

The temporal variation of I_1 , I_2 , and I_3 , is shown figure 4 for the same parameters as in figure 3. For this set of parameters, it can be seen that the magnitude of I_2 is small in comparison to that of the rest of the terms; this implies that the average values of gravity and capillarity play a small role in determining the overall response of the system. The terms I_1 and I_3 are out of phase with one another; the difference in their magnitudes appears to largely determine the sign of the instantaneous growth rate of the film thickness whose average value increases with time. The term I_3 is negative (positive) over the duration in which $GH > 0$ ($GH < 0$), which highlights the fact that Marangoni stresses can be both stabilizing and destabilizing during the same forcing cycle.

3.2. Numerical procedure

The evolution equations, (2.12), (2.13), are solved using a pseudo-spectral code that utilizes fast Fourier transforms (FFT) to discretize the spatial derivatives (typically 256–512 modes) and Gear's method in time. The initial conditions are chosen to be either random perturbations of initially small amplitude, taken from a uniform distribution on $10^{-5}[-1, 1]$, or a monochromatic cosine disturbance. In the former case, we have found that pseudo-random perturbations are rapidly reorganized into coherent, periodic-like structures. Subsequently, the evolution of h and Γ and the associated profiles exhibit only minor quantitative differences from those obtained

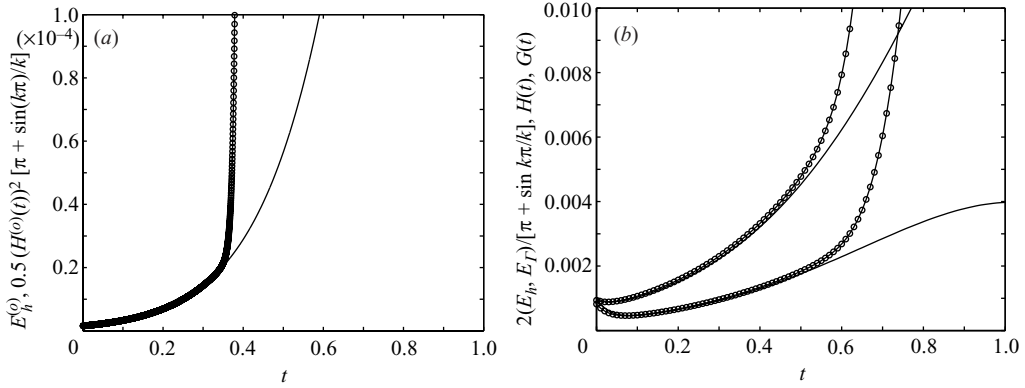


FIGURE 5. Comparison of the numerical solutions (open circles) with linear theory (solid lines), for (a) the clean and (b) contaminated cases. In (a), we plot $E_h^{(o)} = \int_{-\pi/2}^{\pi/2} (h^{(o)} - 1)^2 dx$, a measure of the film ‘energy’, which is generated via numerical solutions of (2.19) and compare this with the analytical solution provided by (3.3); the parameter values are $k=2$, $H^{(o)}(t=0)=10^{-3}$, $\mathcal{A}^{(o)}=3$, $\mathcal{B}^{(o)}=0.16$, and $\mathcal{C}^{(o)}=0.0075$. In (b), the ‘analytical’ solutions have been obtained via numerical solution of (3.4) and (3.5), while the numerical solutions are determined through numerical integration of (2.12) and (2.13) for $k=2$, $\mathcal{A}=10$, and the same parameters as in figure 1(c).

starting from initially monochromatic conditions. In either case, numerical solutions are obtained subject to periodic boundary conditions.

The length of the computational domain is chosen to be from $-\pi$ to π for the majority of the cases considered. Solutions are obtained for the following parameter ranges: $3 \leq \mathcal{A} \leq 10$, $0 \leq \mathcal{M} \leq 100$, $10 \leq Pe \leq 6.3 \times 10^5$ with $\mathcal{B}=0.16$ and $\mathcal{C}=0.0075$ held fixed. The ranges are consistent with orders of magnitude of physical parameters typical of experimental settings (Kumar & Matar 2002).

In order to inspire confidence in the predictions of the numerical procedure, we show in figure 5 a comparison of numerical solutions and the predictions of linear theory for the clean and contaminated cases. The predictions of linear theory correspond to numerical solutions (obtained using Matlab) of (3.4) and (3.5) for the contaminated case, and (3.3) for the clean case. Figure 5 clearly shows that excellent agreement is achieved between linear theory and the numerical solutions at early times for both the clean and contaminated cases, beyond which nonlinearities become significant and (3.3)–(3.5) invalid.

Although one would expect to observe similar trends in the nonlinear regime to those determined using linear theory, detailed knowledge of the dynamics requires accurate numerical solution of (2.12) and (2.13). The results of these computations are discussed next.

3.3. Numerical results: surfactant-free interface

We begin by describing the results generated for the surfactant-free case. In figure 6 we plot the temporal variation of $E_h^{(o)} = \int_{-\pi}^{\pi} (h^{(o)} - 1)^2 dx$, which may be regarded as a measure of the interfacial ‘energy’, for $\mathcal{A}=6$, $k=2$, $\mathcal{B}^{(o)}=0.16$, and $\mathcal{C}^{(o)}=0.0075$ starting from an initially small amplitude of 10^{-3} . Although we have shown, based on Floquet theory, that a surfactant-free interface is stable to initially small-amplitude long-wavelength perturbations, it becomes clear upon inspection of figure 6 that significant growth does occur as a result of nonlinearities. Closer examination of this figure shows several features of interest. The function $E_h^{(o)}$ exhibits a periodic-like

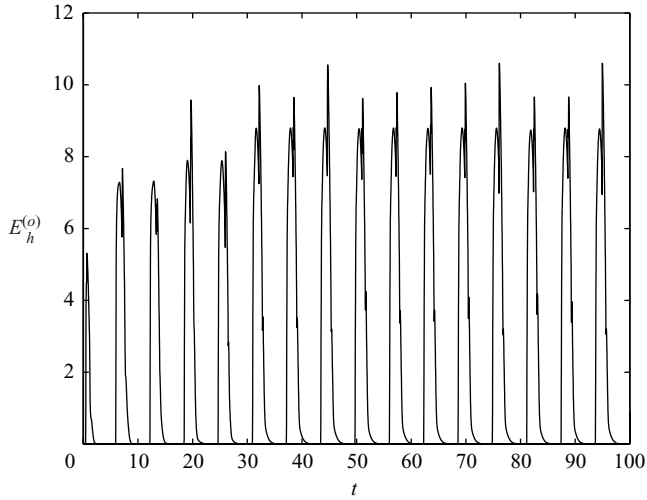


FIGURE 6. Temporal variation of the film ‘energy’, $E_h^{(o)} = \int_{-\pi}^{\pi} (h^{(o)} - 1)^2 dx$, for the uncontaminated case with $\mathcal{A} = 6$, $k = 2$, $\mathcal{B}^{(o)} = 0.16$, and $\mathcal{C}^{(o)} = 0.0075$.

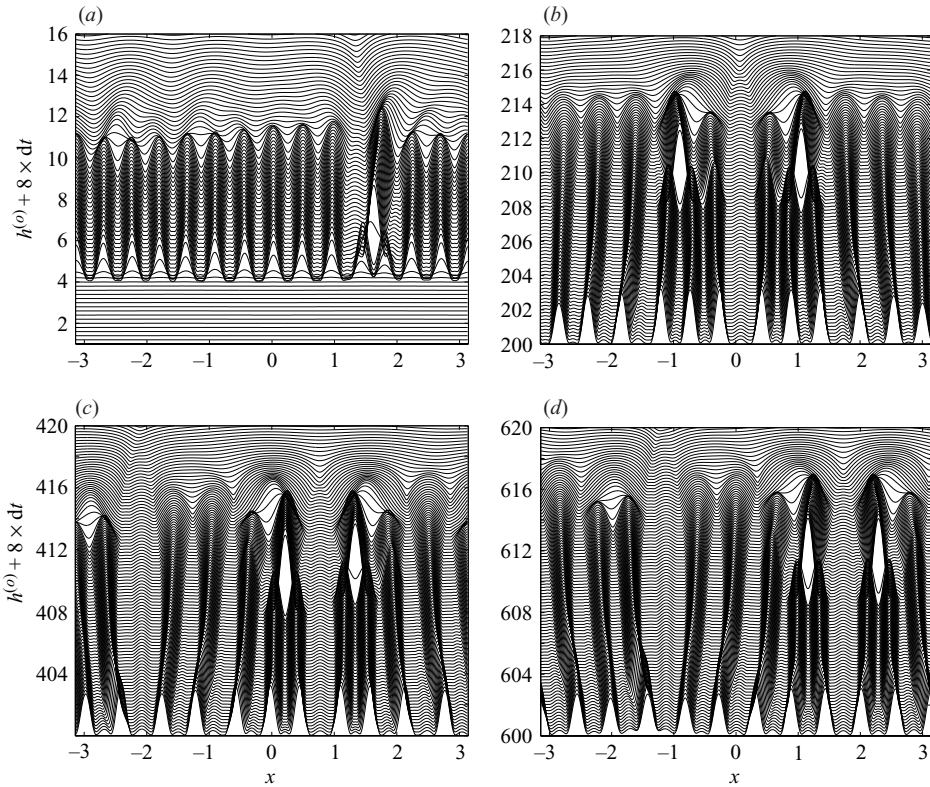


FIGURE 7. Space–time plots of the uncontaminated film thickness, $h^{(o)}$, for the same parameter values as those used to generate figure 6. The ‘cycles’ shown in (a–d) correspond to $t = 0$ –6.25, $t = 6.25$ –12.5, $t = 12.5$ –18.75, and $t = 18.75$ –25, respectively.

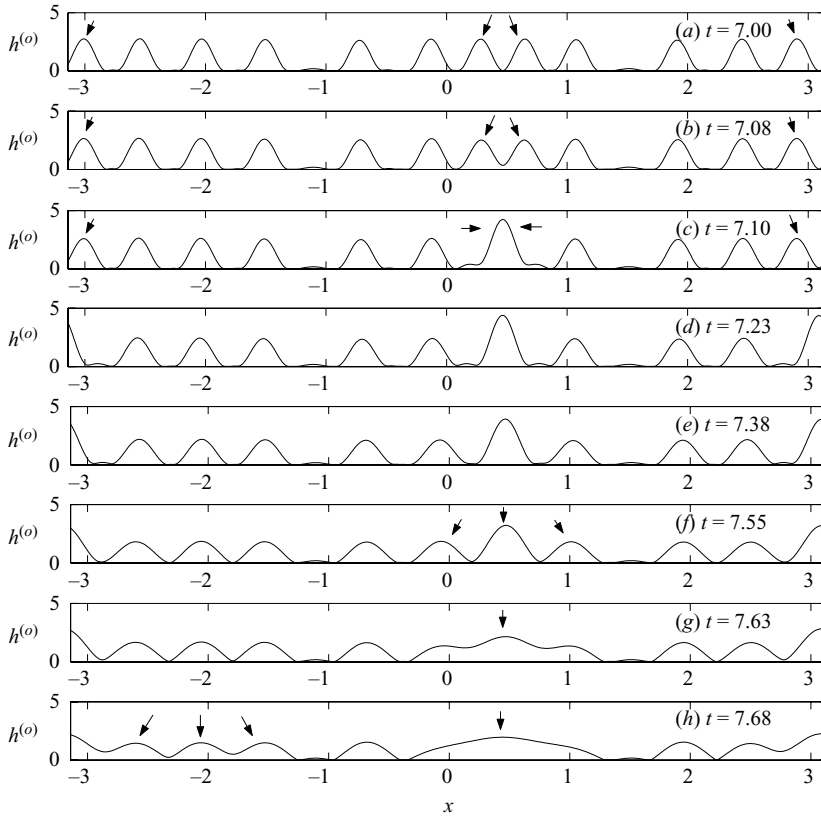


FIGURE 8. A sequence of $h^{(o)}$ profiles showing coalescence events between fluid ridges for the same parameters as in figure 7. Two events, which occur between $t = 7.00$ and $t = 7.38$, are depicted in (a–d), while two more involving three fluid ridges, which take place between $t = 7.38$ and $t = 7.68$, are shown in (e–h). The latter coalescence events result in the formation of fluid mounds, whereas the former give rise to steep ridges. The arrows in each panel indicate the coalescing ridges.

structure with 16 distinct humps reflecting the underlying time-periodic standing-wave structure of the free surface. For all the computations carried out, the first hump was observed to be smaller than the remaining ones. This may be related to the fact that the interface is more unstable following the first ‘cycle’ than at the onset of the flow, which permits larger free-surface amplitudes and, therefore, $E_h^{(o)}$ values to be attained. In each hump, there is a period of large initial growth followed by decay, but there also appear to be several oscillations within each hump. We posit at this stage that these are due to the drifting and subsequent coalescence of large fluid ridges; evidence for this is presented below. It is also worth noting that the system response is harmonic: each hump lasts for an approximate period of 2π , which corresponds to the forcing frequency. This behaviour is consistent with the findings of Muller *et al.* (1997) who predicted analytically and observed experimentally a harmonic surface response in the case of relatively thin viscous films at low forcing frequencies, wherein the damping associated with the underlying solid substrate is significant. We note that their harmonic response arises from linear instability of the full Navier–Stokes equations, whereas ours results from an inherently nonlinear mechanism since our evolution equation is linearly stable.

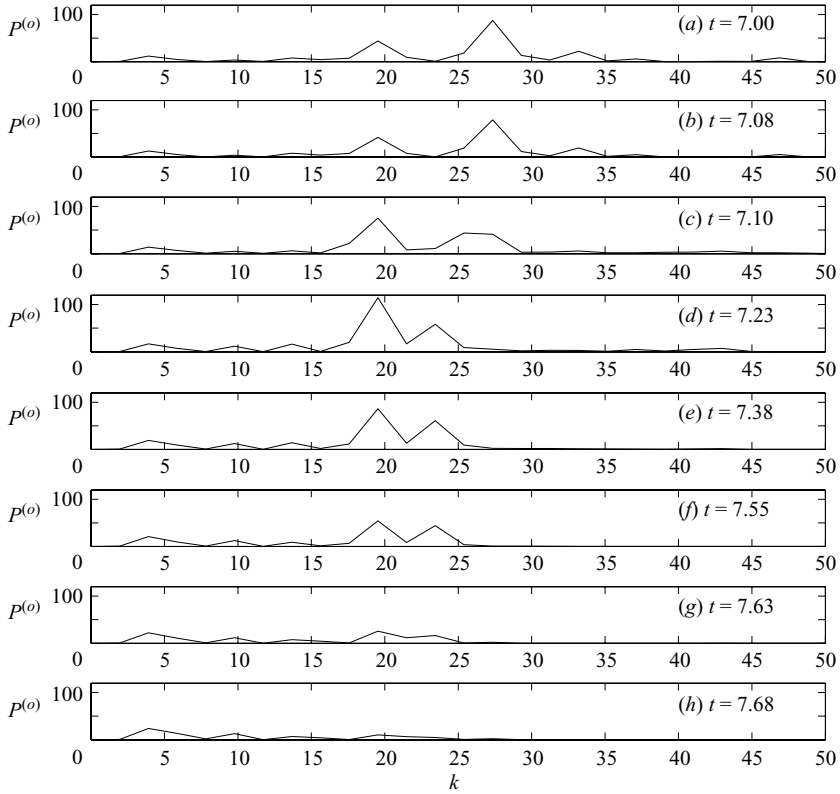


FIGURE 9. A sequence showing the power spectra of $h^{(o)}$, $P^{(o)} = |\hat{H}^{(o)}(k)|/N$, for the same parameters and times as in figure 8. Here, $\hat{H}^{(o)}(k) = \sum_{j=1}^N h^{(o)}(j) \exp(-2\pi i(j-1)(k-1))/N$ is the discrete Fourier transform in which $N = 512$ corresponds to the number of modes used and k is the wavenumber.

In order to illustrate the spatio-temporal evolution of the free-surface, we show in figure 7 space-time plots of $h^{(o)}$ over the first four ‘cycles’ shown in figure 6. Examination of this figure shows the relatively complex evolution of the free surface. Starting from rapid growth of essentially cosine-like disturbances, the dynamics are accompanied by ridge drifting and coalescence, giving rise to larger structures and an overall reduction in the number of ridges. These coalescence events appear to be particularly severe after the first cycle, resulting in ridges with very tall peaks. Qualitatively similar results were determined by Wright *et al.* (2000), who observed the emergence and subsequent collision of travelling waves to form large-amplitude peaks. The development of large peaks was also observed by Ubal *et al.* (2003) via numerical solution of the two-dimensional Navier–Stokes equations.

The occurrence of ridge coalescence is further illustrated in figure 8, in which we show a sequence of $h^{(o)}$ profiles between $t = 7.00$ and $t = 7.68$, corresponding to the time period in which oscillations in $E_h^{(o)}$ are observed in the second cycle in figure 6. Inspection of figure 8(a–d) shows clearly the coalescence of two sets of ridges (highlighted by arrows) to form a large ridge at $t = 7.10$ (see figure 8c) and another at $t = 7.23$ (see figure 8d). Similar events take place between $t = 7.38$ and $t = 7.68$, as shown in figure 8(e–h). The coalescence events involve three rather than two fluid ridges and result in the formation of large mounds of fluid, one of which is clearly shown in panel (h) at $t = 7.68$. The energy values associated with the times shown in

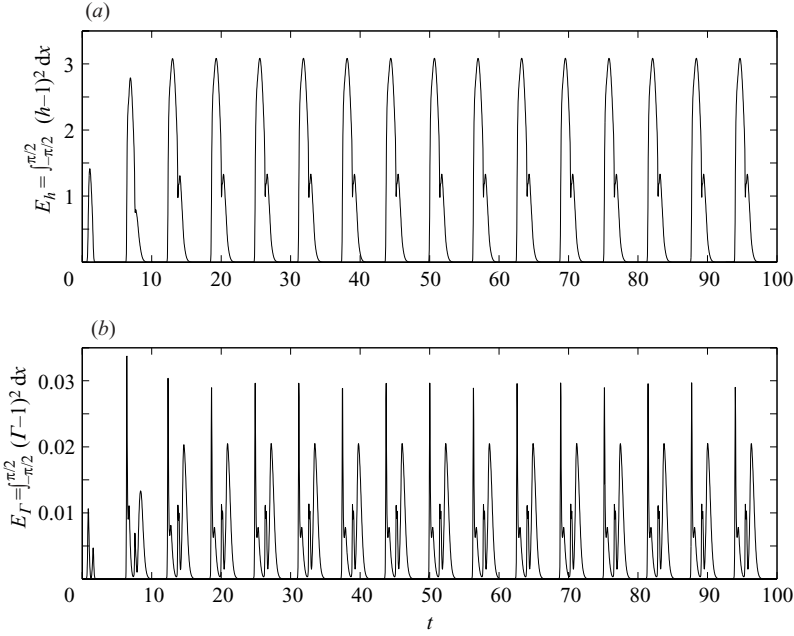


FIGURE 10. Temporal variation of the film and surfactant concentration 'energies', (a) E_h and (b) E_Γ . The parameter values remain unchanged from figure 1(a).

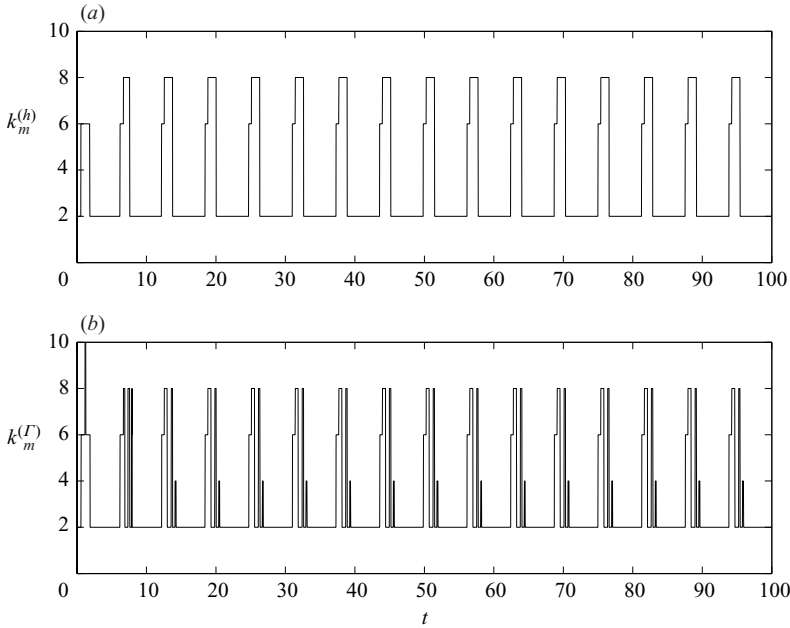


FIGURE 11. Temporal variation of the most dominant modes, (a) $k_m^{(h)}$ and (b) $k_m^{(\Gamma)}$, for h and Γ , for the same parameters as in figure 10. Here, $k_m^{(h)}$ and $k_m^{(\Gamma)}$ correspond to the wavenumbers which maximize the value of $P^{(h)} = |\hat{H}(k)|/N$ and $P^{(\Gamma)} = |\hat{\Gamma}(k)|/N$, respectively, wherein the discrete Fourier transforms of h and Γ are expressed by $\hat{H}(k) = \sum_{j=1}^N h(j) \exp(-2\pi i(j-1)(k-1))/N$ and $\hat{\Gamma}(k) = \sum_{j=1}^N \Gamma(j) \exp(-2\pi i(j-1)(k-1))/N$; here, the number of modes is $N = 256$.

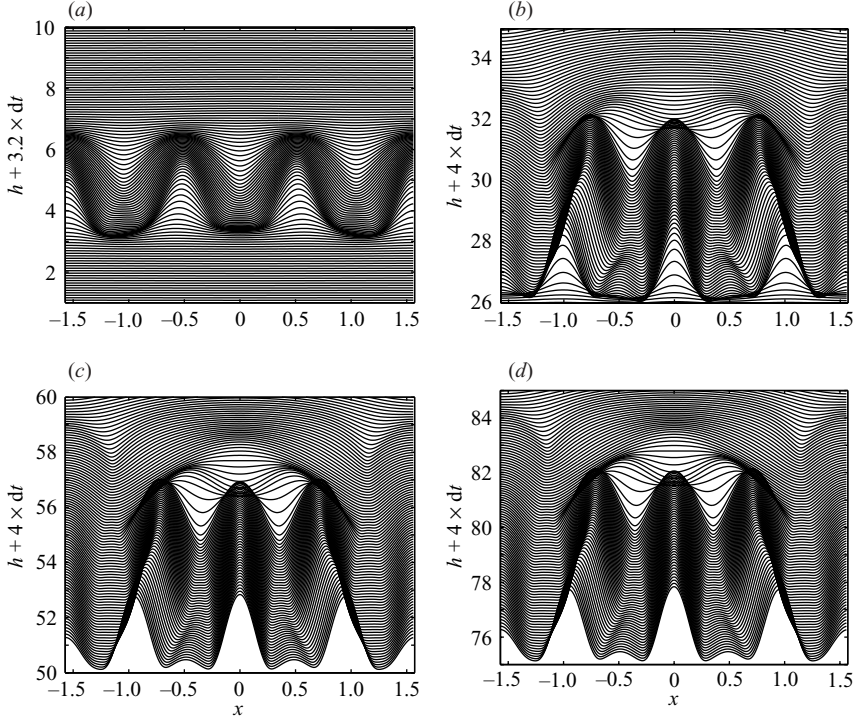


FIGURE 12. Space-time plots of h for the same parameters as in figure 10, showing four ‘cycles’ in panels (a–d) that correspond to $t = 0\text{--}6.25$, $t = 6.25\text{--}12.5$, $t = 12.5\text{--}18.75$, $t = 18.75\text{--}25$, respectively.

figure 8 are $E_h^{(o)} = 6.26, 5.76, 6.61, 7.39, 6.08, 4.23, 2.85$, and 2.19 , respectively, which indicates that the energy decreases during the coalescence process and rises following the formation of the large ridge.

We have shown that the structural evolution of $h^{(o)}$ is accompanied by a change in the overall number of discrete ridges. In order to illustrate this fact more clearly, we plot in figure 9 a sequence of profiles showing the power spectra of $h^{(o)}$, $P^{(o)} = |\hat{H}^{(o)}(k)|/N$, for the same period of time as in figure 8, wherein $\hat{H}^{(o)}(k) = \sum_{j=1}^N h^{(o)}(j) \exp(-2\pi i(j-1)(k-1)/N)$ is the discrete Fourier transform; here $N = 512$ corresponds to the number of modes used to compute the transform and k is the wavenumber. At $t = 7.00$, the wavenumber associated with the dominant mode that maximizes the value of $P^{(o)}$, k_m , is approximately equal to 27. The coalescence process results in a shift of k_m towards smaller values, as shown in figure 9(a–d), which indicates structure coarsening. Further coalescence gives rise to several peaks in the $P^{(o)}$ vs. k plot (see figure 9h), indicating the existence of several modes in Fourier space, which make up the structure observed in figure 8(h).

We have found (not shown) that increasing the value of the vibration amplitude, \mathcal{A} , results in qualitatively similar albeit more complex spatio-temporal evolution with more frequent and dramatic coalescence events. We turn our attention to the case of a surfactant-covered free surface and examine the effects of contamination on the dynamics.

3.4. Numerical results: surfactant-covered interface

Figure 10 depicts the ‘energies’ associated with h and Γ , E_h and E_Γ , for the surfactant-covered free-surface case, obtained for an initial disturbance amplitude of 10^{-3} in

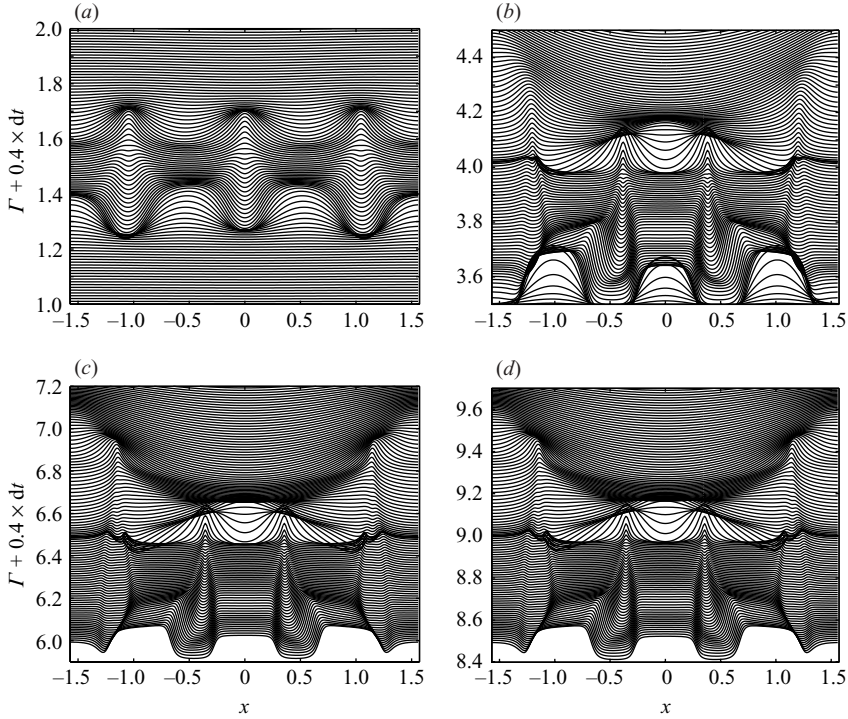


FIGURE 13. Space-time plots of Γ for the same parameters as in figure 10, showing four ‘cycles’ in panels (a–d) that correspond to $t=0-6.25$, $t=6.25-12.5$, $t=12.5-18.75$, $t=18.75-25$, respectively.

h and $k=2$, $\mathcal{A}=10$, $\mathcal{B}=0.16$, $\mathcal{M}=10$, $\mathcal{C}=0.0075$, and $Pe=6.3 \times 10^5$. Inspection of figure 10(a) reveals that E_h exhibits a time-periodic structure with a period approximately equal to 2π , as in the surfactant-free case.

The structure of E_h in figure 10(a) highlights the relative absence of rapid oscillations within individual ‘cycles’ and the overall decrease in the average value of E_h in comparison with figure 6 despite the increase in vibration amplitude from $\mathcal{A}=6$ to $\mathcal{A}=10$. This observation, in turn, indicates the relative absence of coalescence events between fluid ridges. In contrast, E_Γ , shown in figure 10(b), appears to have a more complicated temporal dependence. Although E_Γ has an overall time-periodic structure with a similar period to that of E_h , this function exhibits rapid oscillations during this period, which indicates that Γ has more complex spatio-temporal dynamics than h .

This is further illustrated by figure 11, in which we plot the wavenumber of the dominant Fourier mode for both h and Γ . In the case of h , $k_m^{(h)}$ rises sharply from a base value of $k_m^{(h)}=2$, which corresponds to the wavenumber of the initial condition, $h(x, 0)$, to a value of 6, then 8; this is followed by an equally sharp decay to $k_m^{(h)}=2$ at the end of the cycle. Although the temporal variation of $k_m^{(\Gamma)}$ exhibits a similar initial rise to $k_m^{(\Gamma)}=6$, this is then followed by rapid oscillations culminating in decay to $k_m^{(\Gamma)}=2$ at the end of the cycle. It is also noteworthy that the maximal value of $k_m^{(h)}$ in the contaminated case is significantly lower than the uncontaminated case, indicating the presence of fewer fluid ridges.

In order to examine the spatio-temporal dynamics of h and Γ , we show space-time plots of h and Γ in figures 12 and 13, respectively, for the same parameters as in figure 10. As expected, close inspection of figure 12 reveals that the drifting of ridges

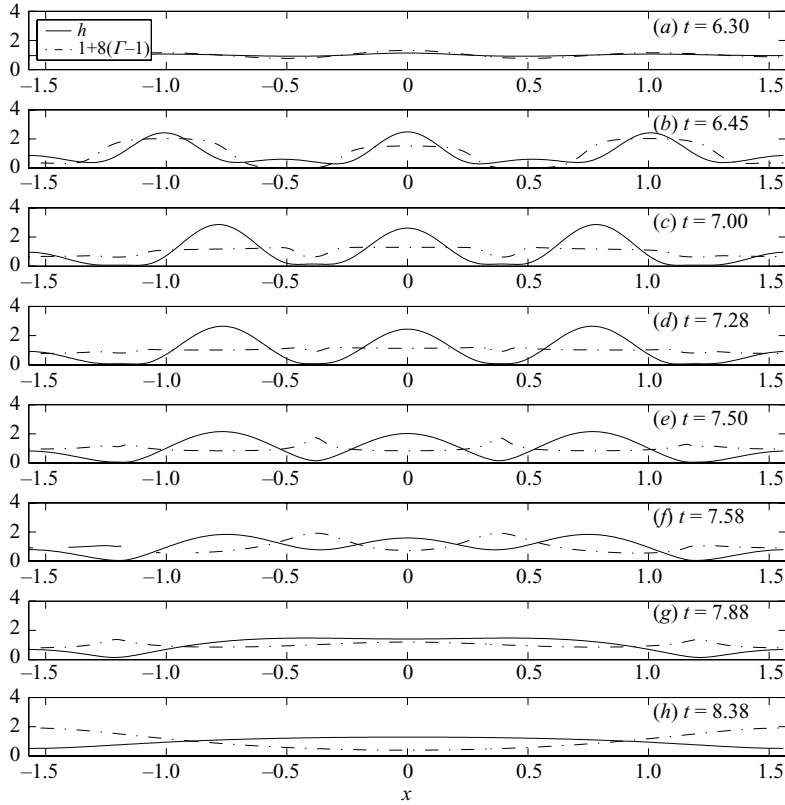


FIGURE 14. A sequence of profiles of the film thickness (solid lines) and surfactant concentration (dot-dashed lines) showing the spatio-temporal evolution of h and Γ between $t = 6.30$ and 8.38 for the same parameters as in figure 12. Here, we have plotted $1 + 8 \times (\Gamma - 1)$ rather than Γ for the surfactant concentration for the sake of clarity.

occurs over slower time scales than in the uncontaminated case, resulting in a single coalescence event at the end of each cycle following the first cycle; this explains the absence of rapid oscillations in figure 10(a). In contrast, the space-time plot associated with Γ , shown in figure 13, is considerably more complicated than that of h . Figure 13(b–d) illustrate that Γ appears to evolve on a more rapid time scale than h : disturbances, which are cosine-like at the beginning of a cycle, rapidly evolve into thickened ridges of surfactant concentration which then merge into a double-humped structure that finally relaxes into a long-wavelength disturbance at the end of the cycle.

It is instructive to study the evolution of h and Γ by examining flow profiles in which these variables are superimposed on one another. Figure 14 depicts a sequence of h and Γ shown between $t = 6.30$ and 8.38 , which corresponds to a time period that lies in the second cycle as shown in figure 10; the rest of the parameter values are the same as in figure 12. Because h achieves much larger values than Γ , which cannot exceed unity, we have plotted $8 \times (\Gamma - 1) + 1$ rather than Γ in figure 14 for the sake of clarity. Inspection of figure 14(a, b) reveals that h and Γ are in phase at the beginning of the cycle with both variables undergoing rapid growth to form thickened ridges starting from essentially cosine-like disturbances. At this stage, therefore, relatively thick fluid regions are coated with a relative excess of surfactant concentration. This then results in a Marangoni-driven flow from high to low concentration regions, which,

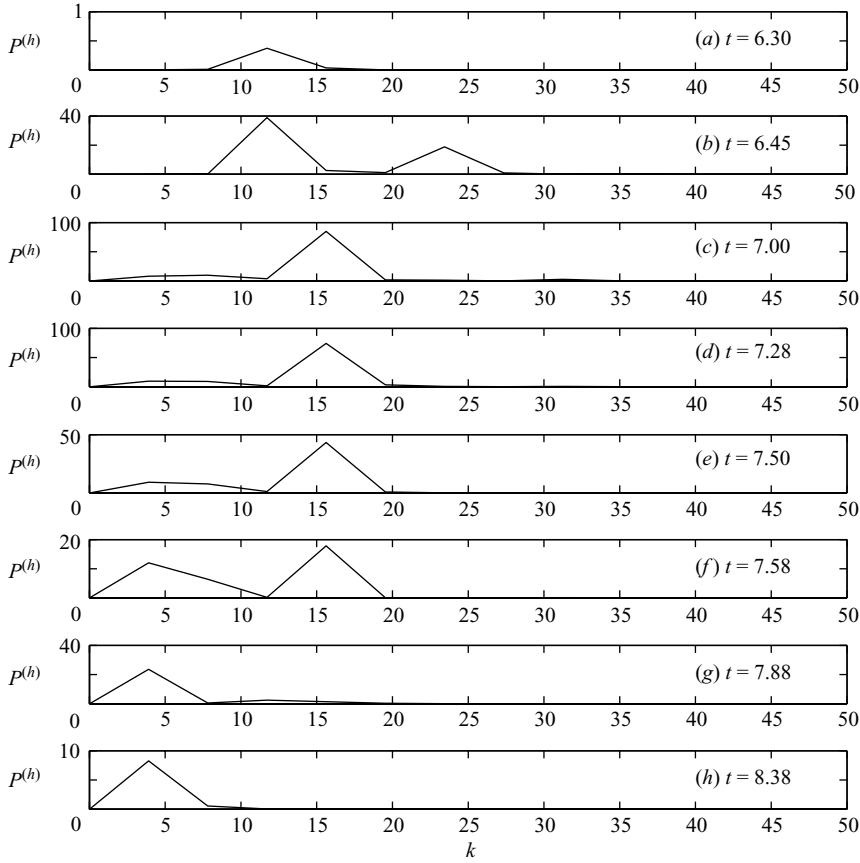


FIGURE 15. A sequence showing the power spectra of h , $P^{(h)}$, for the same parameters as in figure 14. Here, P is defined in the same way as in figure 11 with $N = 256$.

in turn, results in a more uniform concentration profile (see figure 14*c, d*). The system dynamics, however, evolve in such a way so that Γ and h are out of phase, as shown in figure 14(*e, f*). Marangoni stresses then drive flow from high to low concentration regions, which at this stage correspond to troughs and crests, respectively. This in turn results, once again, in a more uniform concentration, as shown in figure 14(*g*). This Marangoni-driven flow rigidifies the interface, counteracting the flow resulting from the coalescence of the fluid ridges which could have resulted in a potentially large-amplitude ridge; instead this amplitude only achieves a value of order 2, which is lower than in the uncontaminated case shown in figure 8 despite the large vibration amplitude used here. Finally, the profile shown in figure 14(*h*) indicates that h and Γ are once again completely out of phase.

The contrast in complexity of the structure of the film thickness and surfactant concentration is also reflected by the power spectra of h and Γ shown in figures 15 and 16, respectively, for the same parameter values as those used to generate figure 14. Following the rapid formation of smaller bumps between the large ridges (see figure 14*b*), which gives rise to two peaks in the power spectrum of h , at $k = 12$ and $k = 24$ (see figure 15*a, b*), the value of $k_m^{(h)}$ remains approximately equal to $k_m^{(h)} = 15$ for 0.5 dimensionless time units, as can be seen in figure 15(*c–e*). This is then followed

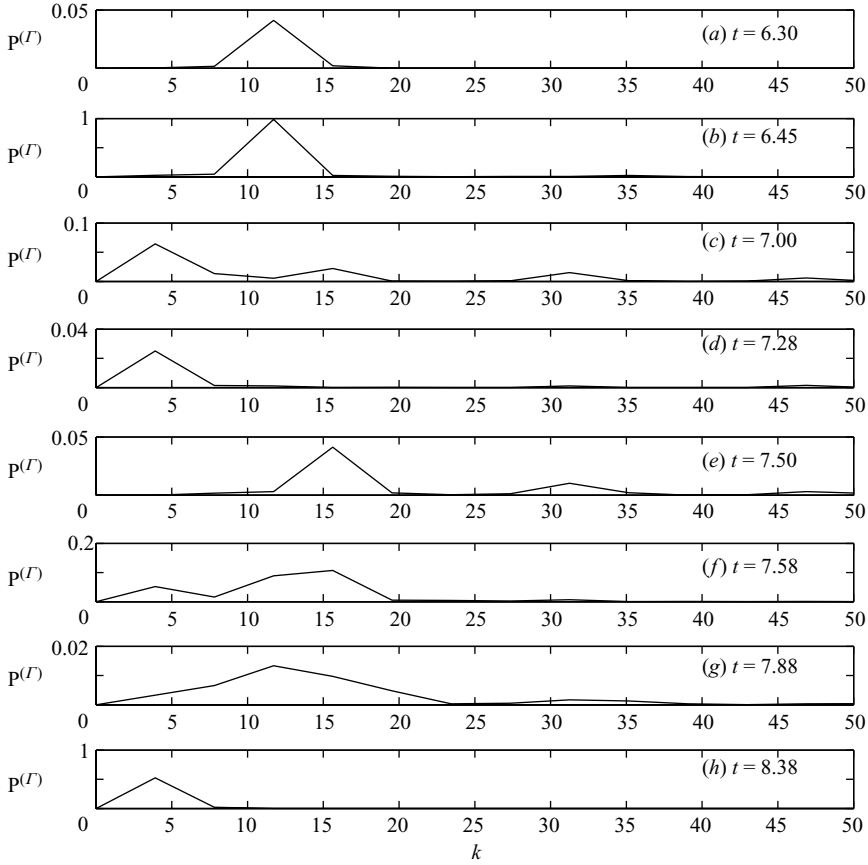


FIGURE 16. A sequence showing the power spectra of Γ , $P^{(\Gamma)}$, for the same parameters as in figure 14. Here, P is defined in the same way as in figure 11 with $N = 256$.

by a relatively slow shift towards $k_m^{(h)} = 4$ over 0.88 dimensionless time units (see figure 15*f–h*). The power spectra of Γ , on the other hand, change constantly following an initially short period of time wherein $k_m^{(\Gamma)} = 12$, which is the same as that of h (see figure 16*a, b*). Of particular interest here is the emergence of fine-scale structure in the dynamics, reflected by the relatively large values of k , which exhibit peaks in the power spectra of Γ ; see, for instance, figure 16(*c, e, g*). The value of $k_m^{(\Gamma)}$ then shifts to that of h at the end of this ‘cycle’, as shown in figure 16(*h*).

We have also examined the effect of lowering \mathcal{M} on the dynamics. This is shown in figure 17 in which we plot the temporal variation of E_h and E_Γ for $\mathcal{M} = 5$ with the rest of the parameter values remaining unaltered from figure 10. A comparison of figures 10 and 17 indicates that although the periodicity of the structure is insensitive to a change in \mathcal{M} , E_h exhibits more frequent rapid oscillations within each ‘cycle’; this is indicative of an increase in the number of coalescence events between fluid ridges. The oscillations in E_Γ , on the other hand, are of similar frequency to those associated with $\mathcal{M} = 10$. Moreover, the maximal amplitudes of both E_h and E_Γ attained in the $\mathcal{M} = 5$ case are larger than those for $\mathcal{M} = 10$. Thus, a decrease in the value of \mathcal{M} is destabilizing due to the reduction in the relative significance of Marangoni stresses, which act to rigidify the interface, suppressing ridge drifting, coalescence, and the subsequent formation of large-amplitude structures.

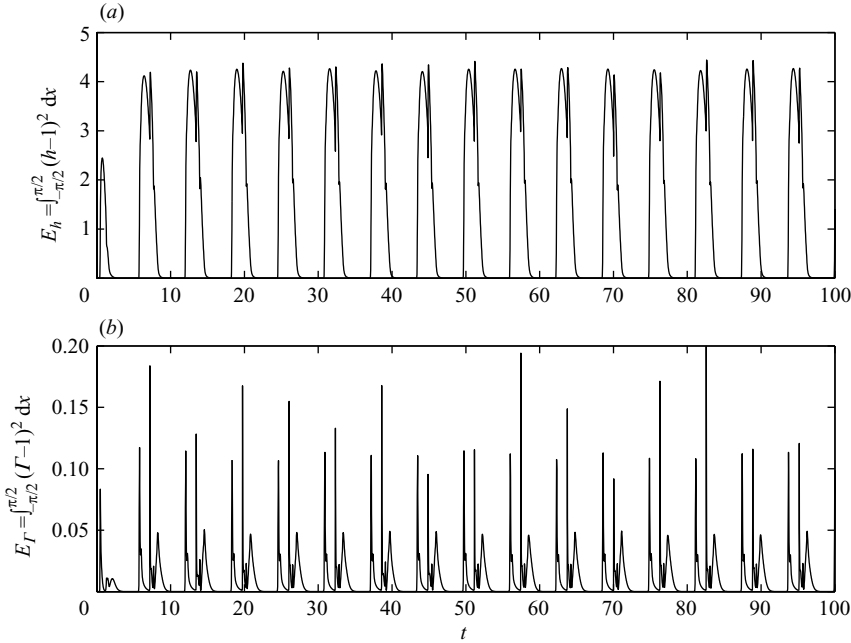


FIGURE 17. Temporal variation of (a) E_h and (b) E_Γ , for the same parameters as in figure 10 except $\mathcal{M} = 5$.

We have investigated the effect of the other system parameters on the dynamics. Increasing the values of \mathcal{B} and \mathcal{C} , which serve to restore both h and Γ to equilibrium, also gives rise to fewer coalescence events and less frequent oscillations in E_h and E_Γ ; these trends are in line with the predictions of linear theory discussed in § 3.2. Finally, variation of Pe , which provides a dimensionless measure of surfactant transport by diffusion, within the range imposed by order of magnitude estimates of the relevant physical quantities, appears to introduce minor quantitative changes to the flow profiles.

4. Concluding remarks

In this work, we have examined the effect of vibration-induced gravity modulation on long-wavelength disturbances on thin liquid films covered with an initially uniform concentration of insoluble surfactant. Spectral methods were used to solve a pair of coupled lubrication-theory-based evolution equations for the film thickness and surfactant concentration which account for the presence of gravitational modulation, capillarity, Marangoni stresses, and surface diffusion. These equations were first derived by Kumar & Matar (2002), who showed using Floquet theory that the presence of surfactant destabilizes an otherwise stable surfactant-free interface, giving rise to standing wave solutions; to the best of our knowledge, such an approach had not been previously adopted in the literature to study this problem. These authors also showed that increasing the relative significance of Marangoni stresses made it more difficult to excite the instability. That study, however, focused on the linear regime and did not examine the nonlinear dynamics of the system. The present work was aimed at addressing this issue.

Although uncontaminated interfaces are linearly stable to long-wavelength disturbances (Kumar & Matar 2002), our results indicate that nonlinear growth can excite unstable flow, leading to the formation of standing waves and a subharmonic response. This flow is accompanied by numerous coalescence events between thickened ridges of fluid, culminating in the formation of large-amplitude pulse-like structures. It may be possible for these events to result in droplet ejections, a possibility which could not be explored within the framework of our thin-film equations.

The interplay between physicochemical and vibration-induced hydrodynamic effects was studied in detail; flow profiles and their power spectra were presented. Despite the fact that the presence of surfactant is destabilizing in a linear sense, the Marangoni stresses associated with this presence were found to exert a rigidifying effect on the interface. This gave rise to less complicated film dynamics, exemplified by ridges of significantly lower amplitude and a drastic reduction in the frequency of coalescence events. In contrast, the surfactant concentration dynamics were found to be more complex than those of the film.

Since the solution of the present model, which involves one-dimensional evolution equations, is considerably easier than that of the two-dimensional Navier–Stokes equations, several extensions of the present work may be worthy of pursuit within the context of thin viscous films. For instance, accounting for surfactant solubility may lead to a dramatic increase in ridge amplitude following a coalescence event; similar steepening of front-like structures was observed by Jensen & Grothberg (1993) in their study of soluble surfactant spreading on thin liquid films. Investigating the effect of film rheology on the dynamics may also be carried out. Obtaining transient numerical solutions of the two-dimensional governing equations would also be of interest, since these would permit the study of stability, dynamics, and pattern formation of two-dimensional standing waves on a surfactant-covered free surface. These solutions could then be used in comparisons with future experiments. Also, the methods developed here and in the work of Kumar & Matar (2002) can be used to study the role of thermocapillarity on surface waves when both temperature gradients and gravity modulation are present, a topic of considerable interest for microgravity applications (Birikh *et al.* 2001; Skarda 2001).

S.K. thanks the Shell Oil Company Foundation for support through its Faculty Career Initiation Funds program and 3M for a Nontenured Faculty Award. R.V.C. and O.K.M. thank the EPSRC for their support through grant number GR/N34895/01.

REFERENCES

- BECHHOEFER, J., EGO, V., MANNEVILLE, S. & JOHNSON, B. 1995 An experimental study of the onset of parametrically pumped surface waves in viscous fluids. *J. Fluid Mech.* **288**, 325–350.
- BENJAMIN, T. B. & URSELL, F. 1954 The stability of the plane free surface of a liquid in vertical periodic motion. *Proc. R. Soc. Lond. A* **225**, 505–515.
- BIRIKH, R. V., BRISKMAN, V. A., CHEREPANOV, A. A. & VELARDE, M. G. 2001 Faraday ripples, parametric resonance, and the Marangoni effect. *J. Colloid Interface Sci.* **238**, 16–23.
- CARPENTER, B. M. & HOMSY, G. M. 1985 The effect of surface contamination on thermocapillary flow in a two-dimensional slot. Part 2. Partially contaminated interfaces. *J. Fluid Mech.* **155**, 429–439.
- CERDA, E., ROJAS, R. & TIRAPEGUI, E. 2000 Asymptotic description of a viscous fluid layer. *J. Statist. Phys.* **101**, 553–565.
- CERDA, E. A. & TIRAPEGUI, E. L. 1998 Faraday's instability in a viscous fluid. *J. Fluid Mech.* **368**, 195–228.

- CHEN, P. 2002 Nonlinear wave dynamics in Faraday instabilities. *Phys. Rev. E* **65**, 036308-1–036308-6.
- DEEN, W. M. 1998 *Analysis of Transport Phenomena*. Oxford University Press.
- EDWARDS, D. A., BRENNER, H. & WASAN, D. T. 1991 *Interfacial Transport Processes and Rheology*. Butterworth-Heinemann.
- FARADAY, M. 1831 On the forms and states assumed by fluids in contact with vibrating elastic surfaces. *Phil. Trans. R. Soc. Lond.* **121**, 319–340.
- JENSEN, O. E. & GROTHBERG, J. B. 1993 The spreading of heat or soluble surfactant along a thin film. *Phys. Fluids A* **5**, 58–68.
- KUMAR, K. 1996 Linear theory of the Faraday instability in viscous liquids. *Proc. R. Soc. Lond. A* **452**, 1113–1126.
- KUMAR, K. & TUCKERMAN, L. S. 1994 Parametric instability of the interface between two fluids. *J. Fluid Mech.* **279**, 49–68.
- KUMAR, S. 1999 Parametrically driven surface waves in viscoelastic liquids. *Phys. Fluids* **11**, 1970–1981.
- KUMAR, S. & MATAR, O. K. 2002 Instability of long-wavelength disturbances on gravity-modulated surfactant-covered thin liquid layers. *J. Fluid Mech.* **466**, 249–258.
- KUMAR, S. & MATAR, O. K. 2004 On the Faraday instability in a surfactant-covered liquid. *Phys. Fluids* **16**, 39–46.
- MILES, J. & HENDERSON, D. 1990 Parametrically forced surface waves. *Annu. Rev. Fluid Mech.* **22**, 143–165.
- MULLER, H. W., WITTMER, H., WAGNER, C., ALBERS, J. & KNORR, K. 1997 Analytic stability theory for Faraday waves and the observation of the harmonic surface response. *Phys. Rev. Lett.* **78**, 2357–2360.
- MURAKAMI, Y. & CHIKANO, M. 2001 Two-dimensional direct numerical simulation of parametrically excited surface waves in viscous fluid. *Phys. Fluids* **13**, 65–74.
- PERLIN, M. & SCHULTZ, W. W. 2000 Capillary effects on surface waves. *Annu. Rev. Fluid Mech.* **32**, 241–274.
- RAYNAL, F., KUMAR, S. & FAUVE, S. 1999 Faraday instability with a polymer solution. *Eur. Phys. J. B* **9**, 175–178.
- SCRIVEN, L. E. & STERNLING, C. V. 1964 On cellular convection driven by surface-tension gradients: effects of mean surface tension and surface viscosity. *J. Fluid Mech.* **19**, 321–340.
- SKARDA, J. R. L. 2001 Instability of a gravity-modulated fluid layer with surface tension variation. *J. Fluid Mech.* **434**, 243–271.
- STONE, H. A. 1990 A simple derivation of the time-dependent convective-diffusion equation for surfactant transport along a deforming interface. *Phys. Fluids A* **2**, 111–112.
- UBAL, S., GIAVEDONI, D. & SAITA, F. A. 2003 A numerical analysis of the influence of the liquid depth on two-dimensional Faraday waves. *Phys. Fluids* **15**, 3099–3113.
- WAGNER, C., MULLER, H. W. & KNORR, K. 1999 Faraday waves on a viscoelastic liquid. *Phys. Rev. Lett.* **83**, 308–311.
- WRIGHT, J., YON, S. & POZRIKIDIS, C. 2000 Numerical studies of two-dimensional Faraday oscillations of inviscid fluids. *J. Fluid Mech.* **402**, 1–32.